


Article

A Feasible and Effective Post-Treatment Method for High-Quality $\text{CH}_3\text{NH}_3\text{PbI}_3$ Films and High-Efficiency Perovskite Solar Cells

Yaxiao Jiang , Limin Tu, Haitao Li, Shaohua Li, Shi-E Yang and Yongsheng Chen *

Key Lab of Material Physics, Department of Physics and Engineering, Zhengzhou University, Zhengzhou 450052, China; JIANGYAX1992@163.com (Y.J.); tulimin12345@163.com (L.T.); 18239940667@163.com (H.L.); 17638164964@163.com (S.L.); yangshie@zzu.edu.cn (S.-E.Y.)

* Correspondence: chysh2003@zzu.edu.cn

Received: 14 December 2017; Accepted: 13 January 2018; Published: 18 January 2018

Abstract: The morphology control of $\text{CH}_3\text{NH}_3\text{PbI}_3$ (MAPbI_3) thin-film is crucial for the high-efficiency perovskite solar cells, especially for their planar structure devices. Here, a feasible and effective post-treatment method is presented to improve the quality of MAPbI_3 films by using methylamine (CH_3NH_2) vapor. This post-treatment process is studied thoroughly, and the perovskite films with smooth surface, high preferential growth orientation and large crystals are obtained after 10 s treatment in MA atmosphere. It enhances the light absorption, and increases the recombination lifetime. Ultimately, the power conversion efficiency (PCE) of 15.3% for the $\text{FTO}/\text{TiO}_2/\text{MAPbI}_3/\text{spiro-OMeTAD}/\text{Ag}$ planar architecture solar cells is achieved in combination with this post-treatment method. It represents a 40% improvement in PCE compared to the best control cell. Moreover, the whole post-treatment process is simple and cheap, which only requires some CH_3NH_2 solution in absolute ethanol. It is beneficial to control the reaction rate by changing the volume of the solution. Therefore, we are convinced that the post-treatment method is a valid and essential approach for the fabrication of high-efficiency perovskite solar cells.

Keywords: perovskite; solar cells; methylamine vapor; post-treatment; low-cost fabrication

1. Introduction

In recent years, hybrid organic-inorganic perovskite solar cells (PSCs) have developed rapidly. The power conversion efficiencies (PCEs) of these PSCs span from 3.8% [1] to a verified PCE of 22.7% [2], stems from a number of remarkable properties, including high absorption coefficient ($\sim 10^4 \text{ cm}^{-1}$) [3,4], low exciton binding energy ($< 100 \text{ meV}$) [5–7], long charge carrier diffusion length (10^2 – 10^5 nm) [8–11] and high charge carrier mobility (10 – $10^2 \text{ cm}^2 \text{ V}^{-1} \text{ s}^{-1}$) [12–15]. In addition, organometallic halide perovskite is suitable for solution and low temperature fabrication, because the precursor material in several organic solvents (dimethyl sulfoxide (DMSO), *N,N*-Methylformamide (DMF), γ -butyrolactone (γ -GBL), etc.) has a perfect solubility [16–19]. Multifarious methods are successfully used to improve the efficiencies of PSCs, including interface engineering [20,21], compositional engineering [22], solvent engineering [23], new materials [24] and device structure modification [25], etc. Among them, which one is more effective is indistinguishable.

To date, the PCE of PSCs has been enhanced by minimizing charge recombination in bulk perovskite film and/or at the interfaces between perovskite and charge transport layers. The reduction of charge recombination in bulk film requires high quality perovskite film with full surface coverage [26–28], large crystal size [15,29,30] and low defect density [31–33]. The post-treatment using a strong Lewis base is a very effective method to improve the quality of lead halide perovskite films [34–42]. In 2014, Zhao et al. [34] first found a room-temperature phase transformation of $\text{CH}_3\text{NH}_3\text{PbI}_3$ induced by ammonia. After one year,

Zhou et al. [35] reported CH_3NH_2 (MA) induced defect-healing (MIDH) of MAPbI_3 perovskite thin films based on the formation of $\text{MAPbI}_3 \cdot x\text{MA}$ intermediate, resulting in an ultra-smooth and dense film with a higher degree of crystallinity and texture. Chih et al. [36] also certified that the post-treatment by MA gas promotes the regrowth of MAPbBr_3 crystallites following the preferred orientations and significantly enhances the film quality and photoluminescence properties. Zhao et al. [38] thoroughly studied the post-treatment process, and provided design rules for the broad, rational extension of this process to new systems and scales. Jiang et al. [39] introduced MA gas to eliminate grain boundaries and gaps, and Jacobs et al. [40] employed a thermally induced recrystallization of MAPbI_3 during the liquidation process to enhance grain size. However, MA gas is supplied mainly through a solid reaction between MAI and KOH powders at room temperature, which is more complex and expensive. In this paper, commercially cheap methylamine solution in absolute ethanol is used directly to supply MA vapor, and the quality of MAPbI_3 perovskite films can be optimized feasibly by changing the post-treatment times in MA atmosphere. Only after 10 s treatment can the perovskite films with surface smoothness, compact structure and preferential orientation in (110) planes be obtained, which obviously improves the photoluminescence properties and carrier extraction efficiency of perovskite. Introducing this post-treatment method in the PSCs fabrication process, the PCE of $\text{FTO}/\text{TiO}_2/\text{MAPbI}_3/\text{spiro-OMeTAD}/\text{Ag}$ planar heterojunction device is increased by 40% compared to the control devices without treatment.

2. Results and Discussion

Figure 1a presents the X-ray diffraction (XRD) spectrum of MAPbI_3 films with different treatment times in MA gas. The XRD patterns of as-deposited MAPbI_3 film without MA gas treating (0 s) exhibits a main peak at 14.2, which is the characteristic of (110) plane in the tetragonal crystal structure, with other peaks corresponding to the (112), (211), (202), (220), (310), (312), (224), and (314) planes in the plot. The positions of these peaks are accorded with the results published previously [29]. The XRD intensity of (110) peak increases seven-fold with 5 s treating and nine-fold with 15 s treating approximately compared to that without MA treating, then decreases, further extending the MA treatment time. However, as shown in Figure 1a, the intensities of (220) and (310) peaks decrease firstly and then increase with prolonging the time. They ultimately reach the minimum value at 5 s treatment. The XRD intensity ratio of (110) and (310) peaks ($I_{(110)}/I_{(310)}$) with MA treatment time is shown in Figure 1b, and a maximum ratio is obtained with 10 s treatment. This suggests that the regrowth of MAPbI_3 crystallites by MA gas treating prefers the formation of (110) planes on the substrate.

The average crystal size of (110) plane deduced from Scherrer Formula is presented in Figure 1b. The crystal size showed a trend of first increasing and then decreasing with MA treatment time, which is similar to the change of $I_{(110)}/I_{(310)}$ ratios. A maximum size of 47 nm is achieved with 10 s treatment, which is about twofold compared to the as-deposited film, indicating that the optimum MA treatment time is 10 s. Figure 1c shows the UV-Visible light absorbance spectra of the corresponding samples. There is a steep cutoff at the wavelength about 785 nm in accordance with a band gap of about 1.58 eV. The light absorbance at the range of 400–550 nm is more sensitive to the MA treatment time, and the largest absorbance is obtained for the sample with 10 s MA treating. The implementation of unreasonable MA treatment time results in a lower absorbance than that of the as-deposited MAPbI_3 film.

Figure 1d illustrates steady-state photoluminescence (PL) measurement of MAPbI_3 films deposited on FTO/TiO_2 substrates. The position of the stable PL emission peaks center at ~768 nm varies with <10 MeV, which is consistent with the optical gap deduced from the absorption spectra. The PL intensity of as-deposited MAPbI_3 film is very high as shown in Figure 1c, suggesting the inefficient carrier transfer at the $\text{TiO}_2/\text{MAPbI}_3$ interface. The PL intensity decreases with MA treatment time from 0 s to 10 s, and then increases with the further treating. In contrast, the PL measurement of MAPbI_3 film treated with ethanol vapor, as shown in Figure A1, remains unchanged regardless of whether the post-processing time of ethanol vapor is 10 s or 30 s. This indicates that the post-treatment of ethanol vapor is not helpful for the properties of MAPbI_3 film or the carrier transfer at $\text{TiO}_2/\text{MAPbI}_3$

interface. MAPbI₃ film treated with 10 s MA exhibits a minimum PL intensity, which is reduced by 50% compared with the film without MA treating (0 s), indicating a more efficient carrier transfer at interface. This is directly related to the (110) preferential orientation of the perovskite film after 10 s post treatment. Wang et al. [43] reported that the preferential orientation of MAPbI₃ perovskite crystal with (110) crystal plane was better for perovskite solar cells, based on synchrotron radiation two-dimensional X-ray grazing incidence diffraction. The crystallographic orientation of the (110) crystal grains is favorable for the propagation of electrons and holes, and the migration rate of the carriers, which facilitates the rapid propagation of electrons and holes along the out-of-plane direction to the electron and hole transport layer. The carriers convert into an effective photocurrent by the electrode collection, thereby enhancing the device's photoelectric conversion performance.

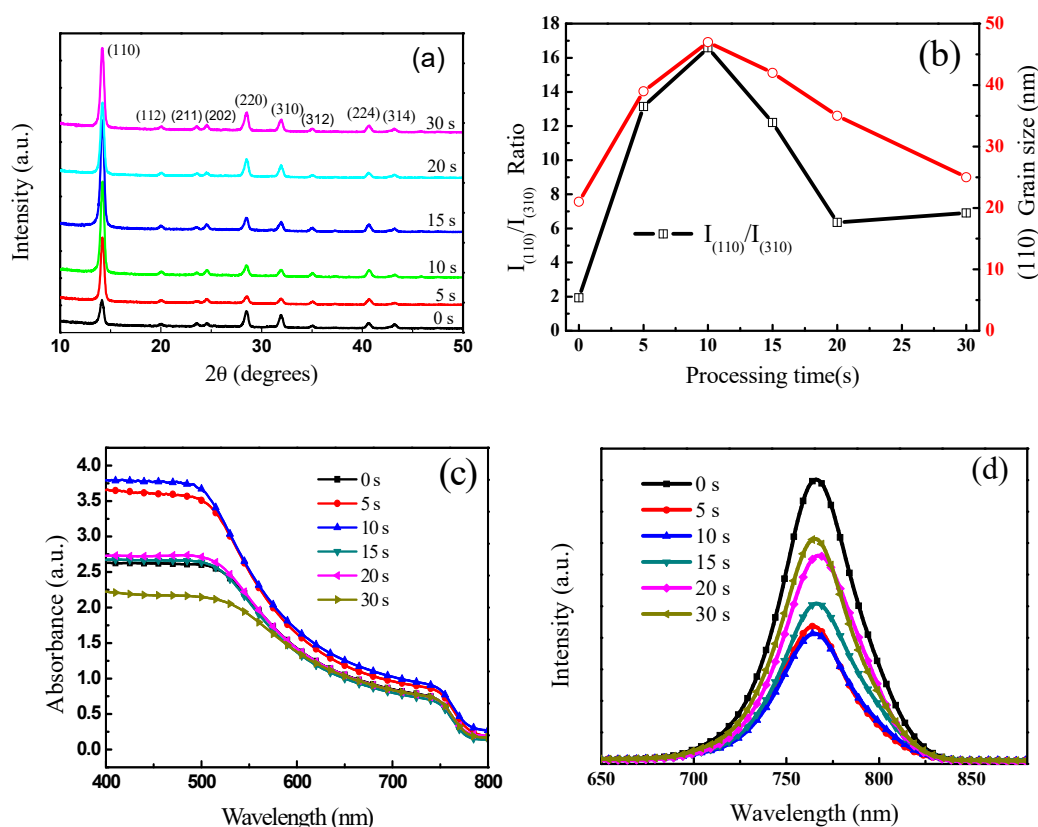


Figure 1. (a) X-ray diffraction (XRD) spectrum and the corresponding; (b) $I_{(110)}/I_{(310)}$ Ratio and the average crystal size of (110) plane of the CH₃NH₃PbI₃ (MAPbI₃) films at different CH₃NH₂ (MA) treatment times; (c) UV-Vis absorption spectra of MAPbI₃ films; and (d) photoluminescence (PL) spectrum of FTO/TiO₂/MAPbI₃ with different times of MA treatment.

The scanning electron microscopy (SEM) images of MAPbI₃ film with different MA gas treatment times are shown in Figure 2a–f (see more data in Figure A2). The as-deposited MAPbI₃ film is composed of densely packed grains with the domain size distributing in a range of 200–300 nm, and the crystal boundaries are visible on the surface of the polycrystalline film, in agreement with the previous report of MAPbI₃ film prepared by the one-step anti-solvent method [44]. After exposing the MAPbI₃ film to MA gas for 5 s, and 10 s, respectively, as shown in Figure 2b–c, the boundary interfaces become unclear, which infers that the gas-solid reaction benefits the regrowth of MAPbI₃ crystallites through the grain boundaries. The corresponding tapping-mode atomic force microscope (AFM) height images in 2.0 μm × 2.0 μm area are presented in Figure 2g–i, and the root-mean-square roughness (RMS) decreases from 7.624 nm for the as-deposited sample to 4.585 nm for the perovskite with 10 s MA treating (three-dimensional images are shown Figure A3). As the post-treatment time increases to 15 s

(Figure 2d), some pinholes appear on the MAPbI₃ film surface. Further increasing the post-processing time to 20 s and 30 s (Figure 2e–f), the MAPbI₃ film is not uniformly covered on the substrate with many voids between grains. Through the low magnification (Figure A2), the film completely covers the substrate when post-processing time is below 15 s. However, if the post-processing time is over 20 s, the substrate is exposed. Therefore, the quality of MAPbI₃ film treated with MA gas is affected by post-processing times.

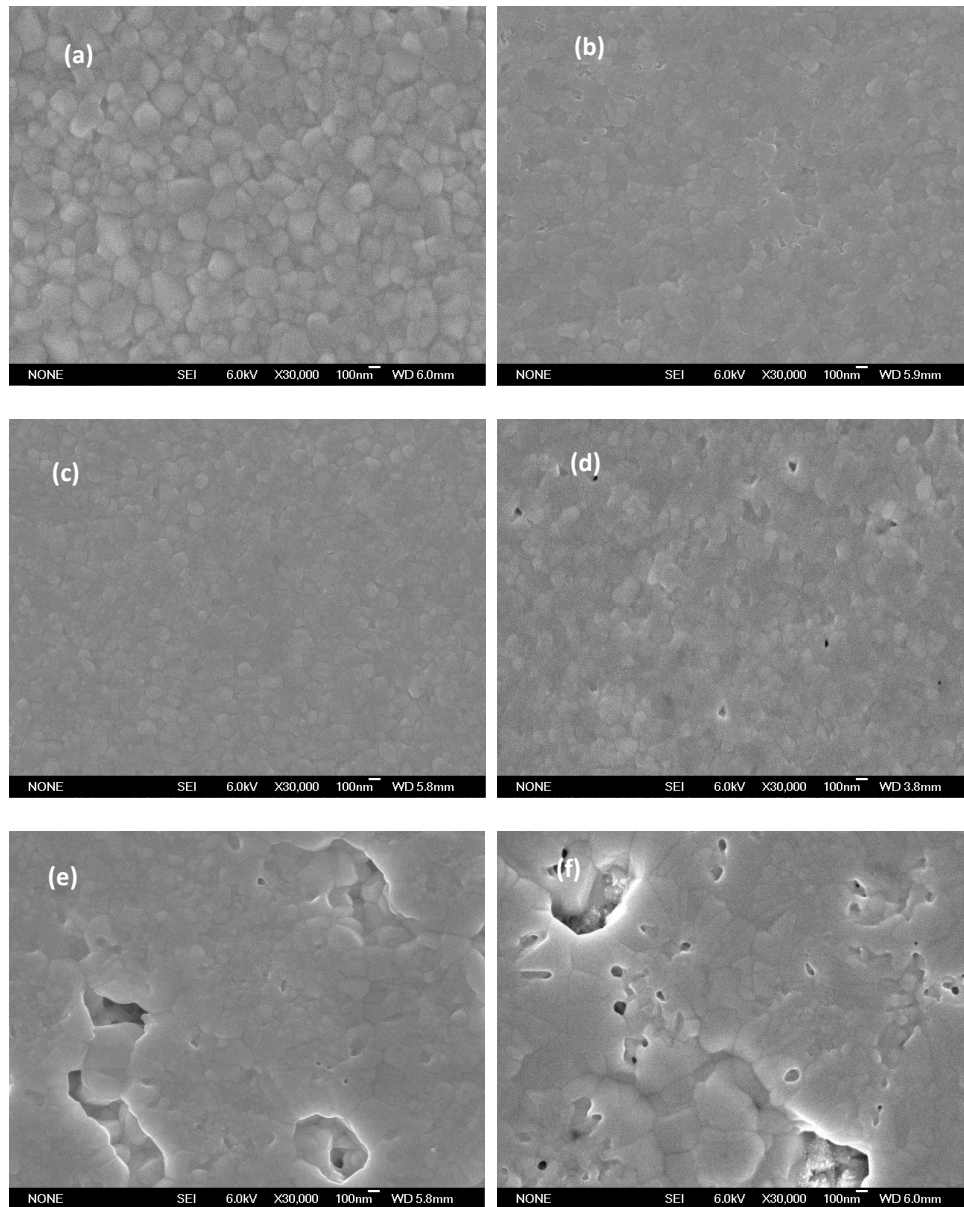


Figure 2. Cont.

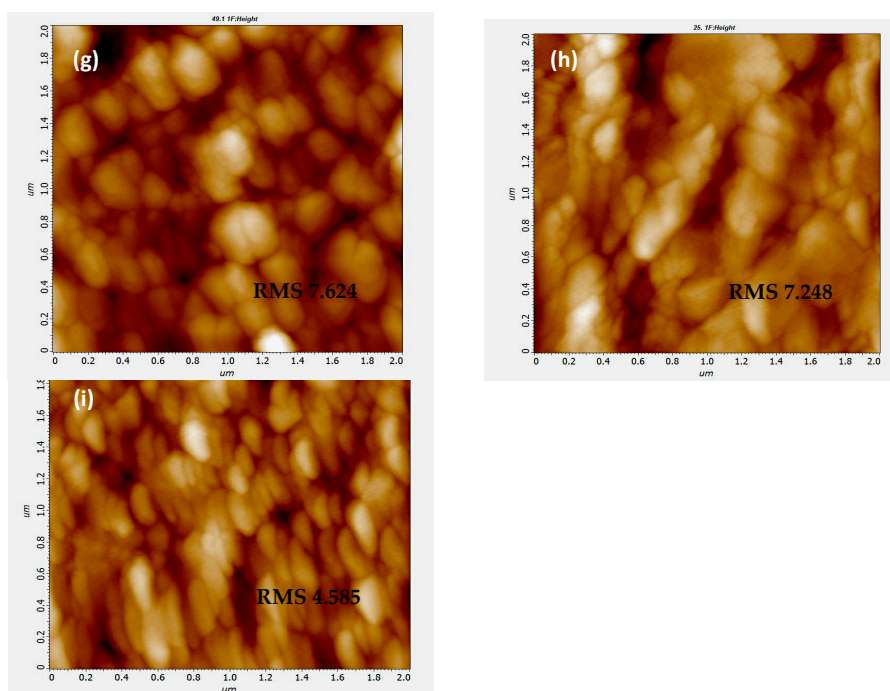


Figure 2. SEM images of MAPbI₃ films at different MA treatment times: (a) 0 s, (b) 5 s, (c) 10 s, (d) 15 s, (e) 20 s, (f) 30 s. Tapping-mode AFM height images of perovskite films treated with MA gas at different times: (g) 0 s, (h) 5 s, (i) 10 s.

Figure 3a depicts the cross-sectional view of the PSC with glass/FTO/TiO₂/MAPbI₃/spiro-OMeTAD/Ag planar structure, in which the thicknesses of TiO₂, MAPbI₃, spiro-OMeTAD, and Ag are about 80 nm, 360 nm, 250 nm, and 100 nm, respectively. Figure 3b shows the J-V characteristic curves of PSCs and the key parameters are listed in Table 1. The PSCs that without MA treating exhibit a J_{SC} of 17.29 ± 0.83 mA/cm², an open-circuit voltage (V_{OC}) of 0.99 ± 0.02 V, and a fill factor (FF) of $59.5 \pm 1.7\%$, leading to a corresponding average PCE of 10.2%. The best device shows a PCE of 10.7% with J_{SC} is 18.1 mA/cm², V_{OC} is 0.98 V, and FF is 60.7%. It is obvious that the low J_{SC} is the main factor that limits the PCE, which is consistent with the reported perovskite solar cell with a similar device structure [45]. For the device with 5 s and 10 s MA treating, J_{SC} and V_{OC} are strikingly enhanced, resulting in an increase in PCE from 12.5% to 14.4%. The best device made of MAPbI₃ layer with 10 s MA treating yields a J_{SC} of 22.1 mA/cm², a V_{OC} of 1.1 V, a FF of 61.5% and a PCE of 15.3%. The crystallinity of perovskite is improved step by step with the increasing of post-treatment times, and the (110) preferred growth is more pronounced (Figure 1a). However, the prolonged MA treatment, 15 s, decreases the performance of devices to an average PCE of 8.9%.

Figure 3c shows the incident photon-to-current conversion efficiency (IPCE) and the integrated product of the EQE curves with the AM1.5G photon flux for the corresponding devices. The J_{SC} data calculated from the IPCE spectra for the devices with 0 s, 5 s, 10 s, and 15 s MA treating is 16.6, 18.4, 20.9, and 15.1 (mA/cm²) respectively, in excellent agreement with the J-V measurements. To check the reproducibility of the device performance, we collected the power conversion efficiency of one batch of devices (25 devices, Figure A4). When the post-treatment time is 10 s, the statistics of the PCEs distribution demonstrates the reliability and repeatability. The results followed a Gaussian distribution with small relative standard deviations.

Furthermore, electrochemical impedance spectroscopy (EIS) is employed to investigate the charge transport processes and recombination dynamics in PSCs. The EIS measurement of PSCs is conducted under 0.6 V applied bias and dark conditions, as shown in Figure 3d. The traditional front high frequency arc has disappeared, confirming that the interface contact capacitance (perovskite/TiO₂ or

spiro-OMeTAD/Ag) is nearly zero. To further understand the impedance spectra, the inset equivalent circuit is used to fit the test results to get detailed information, and the results are listed in Table 1. The difference of R_s is minute, leading to a minor variation of V_{OC} [46]. R_{rec} (recombination resistance) increases with the increase of MA treatment times from 0 s to 10 s, suggesting the significant improvement in electron injection and the effective suppression in charge recombination, resulting in the enhanced device performance. However, once the treatment exceeds 10 s, R_{rec} rapidly decreases, revealing deteriorative electron extraction at the interfaces that directly related to the formation of pinholes in the MAPbI₃ films [47]. These results suggest that the defects at the grain boundaries and the coverage of film are the two crucial parameters that directly affect the device's performance. It is confirmed that the MA treatment method is a very effective process to improve the quality of MAPbI₃ films again. The optimum MA treatment time is 10 s longer than the reported 2–3 s or <1 s [34,37], which is directly involved with the MA gas pressure and the film coverage. So, further optimization of the MA treatment, such as temperature, pressure, etc., is very necessary to obtain high quality thin films and high-performance devices.

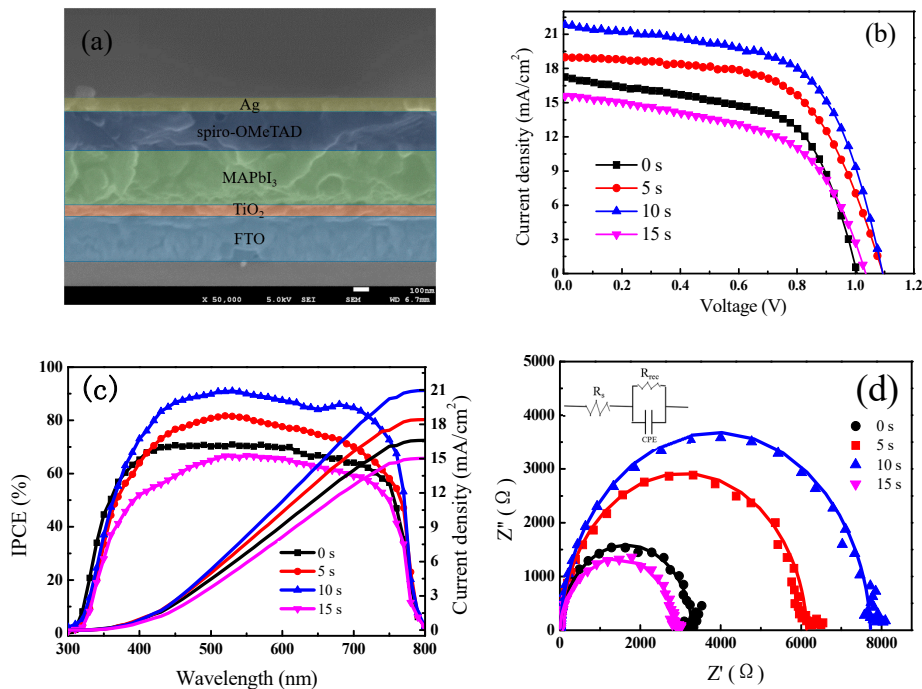


Figure 3. (a) The cross-sectional view of glass/FTO/TiO₂/MAPbI₃/spiro-OMeTAD/Ag planar heterojunction perovskite solar cell; (b) J-V curves and (c) incident photon-to-electron conversion efficiency (IPCE) spectra and integrated current density of the perovskite solar cells (PSCs) at different MA treatment times; (d) The impedance spectra of different MA treatment times of PSCs under 0.6 V applied bias in dark, the inset picture is the equivalent circuit.

Table 1. Parameters of Current Density-Voltage Measurement and Electrochemical Impedance of the PSCs at different MA treatment times.

Time (s)	V_{OC} (V)	J_{SC} (mA/cm ²)	FF (%)	PCE _{ave} (Best) (%)	R_s (Ω cm ²)	R_{rec} (Ω cm ²)
0	0.99 ± 0.02	17.29 ± 0.83	59.5 ± 1.7	10.2 (10.7)	5.8	3265
5	1.09 ± 0.01	19.02 ± 0.63	61.3 ± 1.3	12.5 (13.6)	9.5	6076
10	1.09 ± 0.01	21.85 ± 0.52	61.5 ± 1.2	14.4 (15.3)	8.4	7719
15	1.02 ± 0.01	15.64 ± 0.76	54.5 ± 1.6	8.9 (9.8)	4.1	2876

3. Materials and Methods

3.1. Materials

Dimethylsulfoxide (DMSO), chlorobenzene and *N,N*-Methylformamide (DMF) obtained from Acros Organics. Titanium (IV) Chloride (TiCl_4 , 99.0%) purchased from Kermel (Tianjin, China). Spiro-OMeTAD (99.5%), Li-TFSI (99.95%), 4-*tert*-butyl pyridine (TBP, 96%), Lead (II) Iodide (PbI_2), Methylammonium iodide (MAI) was purchased from Xi'an Polymer Light Technology Corp (Xi'an, China). Methylamine solution in absolute ethanol (38 wt %) was purchased from Sigma Aldrich (Shanghai, China). All the chemicals were directly used without further purification.

3.2. Fabrication of Perovskite Solar Cells

The FTO was wiped with a cotton swab dipped in glass cleaner and then cleaned ultrasonically for 20 min in deionized water, acetone, alcohol and isopropanol orderly. Finally, the washed FTO substrates were treated with UV for 10 min.

Preparation of TiO_2 blocking layer by chemical bath deposition method: the cooled TiCl_4 (99.9%) solution of 2200 μL was added dropwise to ice-water of 100 mL (Divided by 22 times, each time added dropwise 100 μL). Then the solution stirred for another 30 min to prepare a homogeneous solution at a concentration of 200 mM. The FTO substrates were immersed into the precursor solution and kept in an oven at 70 °C for 50 min. After 50 min, the FTO substrates were washed with water and ethanol and then dried at 100 °C in air for an hour.

Lead iodide (PbI_2) and methyl ammonium iodide (MAI) were dissolved in organic solvent (DMSO:DMF = 3:7, *v/v*) with molar ratio of 1:1, stirred in an N_2 filled glove box at 65 °C for 12 h. A yellow precursor solution of methylamine lead iodine at a concentration of 1.25 M was obtained. The spin-coating procedure was performed in the glovebox: first, 700 rpm for 15 s; second, 3000 rpm for 25 s, then anti-solvent chlorobenzene was dropped onto the spinning substrates 18 s after the start of the 3000 rpm spin stage. Finally, the film was annealed at 60 °C for 3 min, 80 °C for 5 min, and 100 °C for 10 min to obtain MAPbI_3 film (Figure 4).

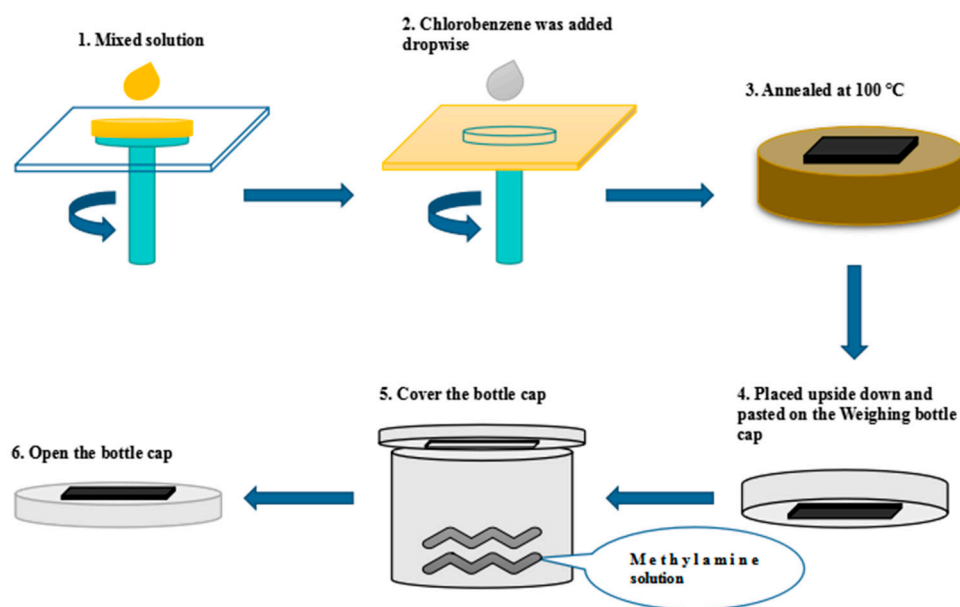


Figure 4. The schematic drawing illustrates the process to prepare MAPbI_3 polycrystalline film and the setup to vapor treatment process.

A portion of the prepared MAPbI₃ films were taken out randomly and subjected to post-treatment in MA vapor. Then we added 80 μ L of Methylamine solution in absolute ethanol into the middle of the weighing bottle (50.60 mL). MAPbI₃ film was placed upside down and pasted on the weighing bottle cap. When the cap was covered, the black MAPbI₃ film immediately became colorless. Then we started timing. The post-processing times were 5 s, 10 s, 15 s, 20 s, 30 s. We opened the bottle cap to stop the process and the colorless film immediately turned black (Figure 4). As a comparison, 80 μ L of ethanol was dropped into the middle of the weighing bottle, but black MAPbI₃ film did not become colorless in 5 s, 10 s, 15 s, 20 s or 30 s (Figure A5).

The hole transporting layer was deposited by spin coating at 3000 rpm for 30 s. The spin-coating formulation was prepared by dissolving 72.5 mg of (2,2,7,7-tetrakis (*N,N*-dip-methoxyphenylamine)-9,9-spirobifluorene) (spiro-OMeTAD) powder in Chlorobenzene solution (1 mL), and then 17.5 μ L of a lithium salt solution (the concentration was 520 mg/mL, the solvent was acetonitrile) was added, followed by the addition of 28.5 μ L of 4-tert-butylpyridine (TBP). Finally, silver electrodes were deposited on the hole transporting layer.

3.3. Instruments

The phase structure was characterized on a Rigaku (D/MAX-2400) X-ray diffractometer (Cu K α radiation, $\lambda = 1.5425$ Å). Scanning electron microscopy (SEM) images were obtained via a field emission scanning electron microscope (JSM-6700F) (JEOL, Tokyo, Japan). Ultraviolet-visible absorption spectra were recorded on a Shimadzu UV-3150 spectrophotometer in the 400–800 nm wavelength range at room temperature. The surface roughness of the films was obtained by atomic force microscopy (AFM, SII Nano Technology Ltd., Nanonavi, Shanghai, China) in noncontact mode. Steady-state photoluminescence (PL) spectra were measured on a FluoroMax-4 Spectrophotometer, using a pulsed diode laser as an excitation source. The current density-voltage (J-V) characteristics were recorded with a Keithley 2400 source meter and 300 W collimated Xenon lamp (Newport) calibrated with the light intensity to 100 mW cm^{−2} under AM1.5G solar light conditions by the certified silicon solar cell. Incident photon-to-electron conversion efficiency (IPCE) was obtained on a computer-controlled IPCE system (Newport) containing a Xenon lamp, a monochromator and Keithley multimeter. Electrochemical impedance spectroscopy was measured using an IM6e Electrochemical Workstation (ZAHENR, Kronach, Germany), in the dark and at 0.6 V, with the frequency ranging between 100 KHz and 0.1 Hz. The Z-View software (Scribner Associates Inc., Southern Pines, NC, USA) was used to fit the impedance spectra.

4. Conclusions

In conclusion, we demonstrate a feasible and effective post-treatment method using MA vapor for improving the quality of MAPbI₃ films. MA treatment can repair the micro-gaps between grains, and eliminate the negative effect of pinhole and grain boundary on the device performance. This is benefit for improving the surface morphology, microstructure, and photo-electrical properties of MAPbI₃ films varied along with the treatment times in MA vapor. XRD and SEM results show that the MAPbI₃ films with surface smoothness, compact structure and preferential orientation in (110) planes can be obtained after 10 s treatment. Under this processing condition, the migration rate of the carriers is enhanced and the absorbance of the MAPbI₃ film is increased through the optical performance test. As a result, the best efficiency of 15.3% is achieved with J_{SC} of 22.1 (mA/cm²), V_{OC} of 1.1 V, FF of 61.5%. Considering that MA vapor is introduced by commercially cheap methylamine ethanol solution, it is expected that this feasible and effective post-treatment method will benefit the easy-control and low-cost fabrication of highly efficient perovskite solar cells.

Acknowledgments: This work was supported by the National Natural Science Foundation of China (61574129), and Basic and Advanced Technology Research Project of Henan Province of China (152300410035).

Author Contributions: Yongsheng Chen and Shi-E Yang conceived and designed the experiments; Yaxiao Jiang performed the experiments; Limin Tu and Haitao Li analyzed the data; Shaohua Li contributed reagents/materials/analysis tools; Yaxiao Jiang wrote the paper.

Conflicts of Interest: The authors declare no conflict of interest.

Appendix A

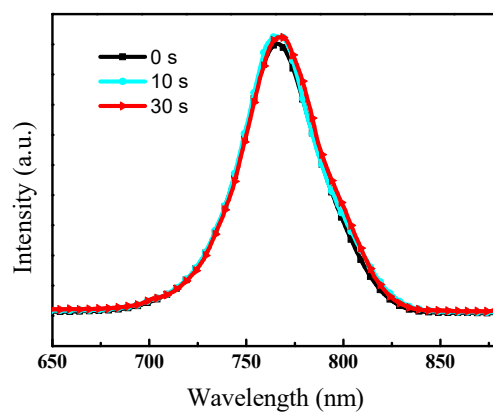


Figure A1. PL spectrum of FTO/TiO₂/MAPbI₃ with different ethanol vapor treatment times.

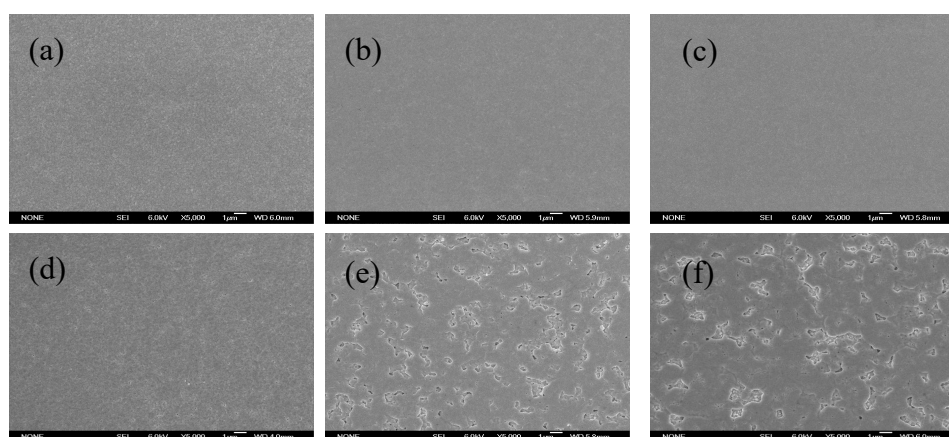


Figure A2. SEM image of MAPbI₃ films at low magnification with different MA treatment times. Processing time: (a) 0 s, (b) 5 s, (c) 10 s, (d) 15 s, (e) 20 s, (f) 30 s.

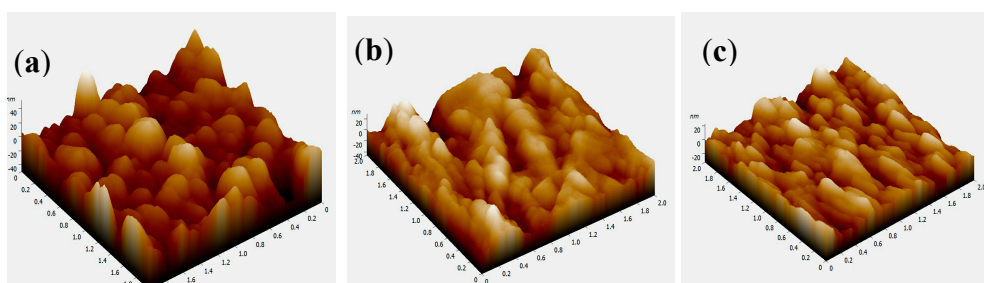


Figure A3. AFM three-dimensional images of perovskite films with different MA treatment times: (a) 0 s (b) 5 s (c) 10 s.

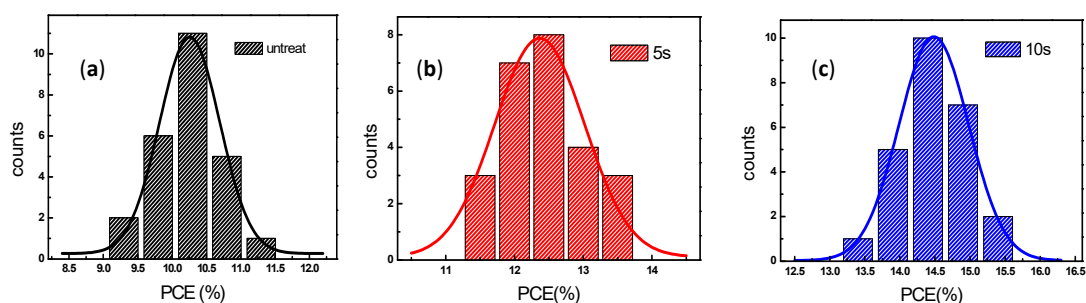


Figure A4. Histograms of PCEs measured for 25 cells that MA gas treating with different times. Processing time: (a) 0 s, (b) 5 s, (c) 10 s.

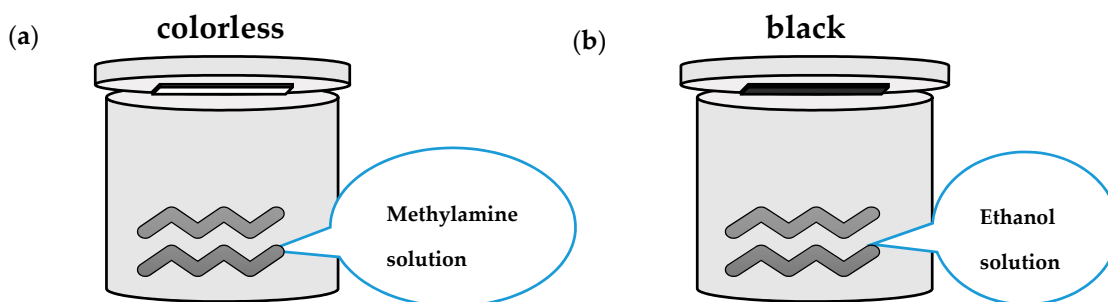


Figure A5. The schematic drawing illustrates the difference to the MA vapor treatment (a) and the ethanol vapor treatment (b).

References

1. Kojima, A.; Teshima, K.; Shirai, Y.; Miyasaka, T. Organometal halide perovskites as visible-light sensitizers for photovoltaic cells. *J. Am. Chem. Soc.* **2009**, *131*, 6050–6051. [CrossRef] [PubMed]
2. National Renewable Energy Laboratory. Best Research-Cell Efficiencies. Available online: <https://www.nrel.gov/pv/assets/images/efficiency-chart.png> (accessed on 30 October 2017).
3. Park, N.-G. Perovskite solar cells: An emerging photovoltaic technology. *Mater. Today* **2015**, *18*, 65–72. [CrossRef]
4. Xie, Z.; Liu, S.; Qin, L.; Pang, S.; Wang, W.; Yan, Y.; Yao, L.; Chen, Z.; Wang, S.; Du, H.; et al. Refractive index and extinction coefficient of $\text{CH}_3\text{NH}_3\text{PbI}_3$ studied by spectroscopic ellipsometry. *Opt. Mater. Express* **2015**, *5*, 29–43.
5. Ishihara, T. Optical properties of PbI_2 -based perovskite structures. *J. Lumin.* **1994**, *60*, 269–274. [CrossRef]
6. Lin, Q.; Armin, A.; Nagiri, R.C.R.; Burn, P.L.; Meredith, P. Electro-optics of perovskite solar cells. *Nat. Photonics* **2015**, *9*, 106–112. [CrossRef]
7. Miyata, A.; Mitiglu, A.; Plochocka, P.; Portugall, O.; Wang, J.T.-W.; Stranks, S.D.; Snaith, H.J.; Nicholas, R.J. Direct measurement of the exciton binding energy and effective masses for charge carriers in organic-inorganic tri-halide perovskites. *Nat. Phys.* **2015**, *11*, 582–587. [CrossRef]
8. Xing, G.; Mathews, N.; Sun, S.; Lim, S.S.; Lam, Y.M.; Grätzel, M.; Mhaisalkar, S.; Sum, T.C. Long-range balanced electron- and hole-transport lengths in organic-inorganic $\text{CH}_3\text{NH}_3\text{PbI}_3$. *Science* **2013**, *342*, 344–347. [CrossRef] [PubMed]
9. Stranks, S.D.; Eperon, G.E.; Grancini, G.; Menelaou, C.; Alcocer, M.J.P.; Leijtens, T.; Herz, L.M.; Petrozza, A.; Snaith, H.J. Electron-hole diffusion lengths exceeding 1 μm in an organometal trihalide perovskite absorber. *Science* **2013**, *342*, 341–344. [CrossRef] [PubMed]
10. Edri, E.; Kirmayer, S.; Henning, A.; Mukhopadhyay, S.; Gartsman, K.; Rosenwaks, Y.; Hodes, G.; Cahen, D. Why lead methylammonium tri-iodide perovskite-based solar cells require a mesoporous electron transporting scaffold (but not necessarily a hole conductor). *Nano Lett.* **2014**, *14*, 1000–1004. [CrossRef] [PubMed]

11. Dong, Q.; Fang, Y.; Shao, Y.; Mulligan, P.; Qiu, J.; Cao, L.; Huang, J. Electron-hole diffusion lengths $>175\ \mu\text{m}$ in solution-grown $\text{CH}_3\text{NH}_3\text{PbI}_3$ single crystals. *Science* **2015**, *347*, 967–970. [[CrossRef](#)] [[PubMed](#)]
12. Ponseca, C.S., Jr.; Savenije, T.J.; Abdellah, M.; Zheng, K.; Yartsev, A.; Pascher, T.; Harlang, T.; Chabera, P.; Pullerits, T.; Stepanov, A.; et al. Organometal halide perovskite solar cell materials rationalized: Ultrafast charge generation, high and microsecond-long balanced mobilities, and slow recombination. *J. Am. Chem. Soc.* **2014**, *136*, 5189–5192. [[CrossRef](#)] [[PubMed](#)]
13. Stoumpos, C.C.; Malliakas, C.D.; Kanatzidis, M.G. Semiconducting tin and lead iodide perovskites with organic cations: Phase transitions, high mobilities, and near-infrared photoluminescent properties. *Inorg. Chem.* **2013**, *52*, 9019–9038. [[CrossRef](#)] [[PubMed](#)]
14. Leijtens, T.; Stranks, S.D.; Eperon, G.E.; Lindblad, R.; Johansson, E.M.J.; McPherson, I.J.; Rensmo, H.; Ball, J.M.; Lee, M.M.; Snaith, H.J. Electronic properties of meso-superstructured and planar organometal halide perovskite films: Charge trapping, photodoping, and carrier mobility. *ACS Nano* **2014**, *8*, 7147–7155. [[CrossRef](#)] [[PubMed](#)]
15. Wehrenfennig, C.; Eperon, G.E.; Johnston, M.B.; Snaith, H.J.; Herz, L.M. High charge carrier mobilities and lifetimes in organolead trihalide perovskites. *Adv. Mater.* **2014**, *26*, 1584–1589. [[CrossRef](#)] [[PubMed](#)]
16. Jeng, J.-Y.; Chiang, Y.-F.; Lee, M.-H.; Peng, S.-R.; Guo, T.-F.; Chen, P.; Wen, T.-C. $\text{CH}_3\text{NH}_3\text{PbI}_3$ perovskite/fullerene planar-heterojunction hybrid solar cells. *Adv. Mater.* **2013**, *25*, 3727–3732. [[CrossRef](#)] [[PubMed](#)]
17. Xiao, Z.; Dong, Q.; Bi, C.; Shao, Y.; Yuan, Y.; Huang, J. Solvent annealing of perovskite-induced crystal growth for photovoltaic-device efficiency enhancement. *Adv. Mater.* **2014**, *26*, 6503–6509. [[CrossRef](#)] [[PubMed](#)]
18. Etgar, L.; Gao, P.; Qin, P.; Graetzel, M.; Nazeeruddin, M.K. A hybrid lead iodide perovskite and lead sulfide QD heterojunction solar cell to obtain a panchromatic response. *J. Mater. Chem. A* **2014**, *2*, 11586–11590. [[CrossRef](#)]
19. Jeon, N.J.; Noh, J.H.; Kim, Y.C.; Yang, W.S.; Ryu, S.; Seok, S.I. Solvent engineering for high-performance inorganic–organic hybrid perovskite solar cells. *Nat. Mater.* **2014**, *13*, 897–903. [[CrossRef](#)] [[PubMed](#)]
20. Zhou, H.; Chen, Q.; Li, G.; Luo, S.; Song, T.-B.; Duan, H.-S.; Hong, Z.; You, J.; Liu, Y.; Yang, Y. Interface engineering of highly efficient perovskite solar cells. *Science* **2014**, *345*, 542–546. [[CrossRef](#)] [[PubMed](#)]
21. Subbiah, J.; Mitchell, V.D.; Hui, N.K.C.; Jones, D.J.; Wong, W.W.H. A Green Route to Conjugated Polyelectrolyte Interlayers for High-Performance Solar Cells. *Angew. Chem. Int. Ed.* **2017**, *56*, 8431–8434. [[CrossRef](#)] [[PubMed](#)]
22. Jeon, N.; Noh, J.; Yang, W.S.; Kim, Y.C.; Ryu, S.; Seo, J.; Seok, S.I. Highly efficient planar perovskite solar cells through band alignment engineering. *Nature* **2015**, *517*, 476–480. [[CrossRef](#)] [[PubMed](#)]
23. Jeon, N.J.; Noh, J.H.; Kim, Y.C.; Yang, W.S.; Ryu, S.; Seok, S.I. Highly efficient and stable planar perovskite solar cells with reduced graphene oxide nanosheets as electrode interlayer. *Nat. Mater.* **2014**, *13*, 897–903. [[CrossRef](#)] [[PubMed](#)]
24. Yang, W.S.; Noh, J.H.; Jeon, N.J.; Kim, Y.C.; Ryu, S.; Seok, S.I. High-performance photovoltaic perovskite layers fabricated through intramolecular exchange. *Science* **2015**, *348*, 1234–1237. [[CrossRef](#)] [[PubMed](#)]
25. Hwang, K.; Jung, Y.-S.; Heo, Y.-J.; Scholes, F.H.; Watkins, S.E.; Subbiah, J.; Jones, D.J.; Kim, D.-Y.; Kim, D.V. Toward Large Scale Roll-to-Roll Production of Fully Printed Perovskite Solar Cells. *Adv. Mater.* **2015**, *27*, 1241–1247. [[CrossRef](#)] [[PubMed](#)]
26. Eperon, G.E.; Burlakov, V.M.; Docampo, P.; Goriely, A.; Snaith, H.J. Morphological control for high performance, solution-processed planar heterojunction perovskite solar cells. *Adv. Funct. Mater.* **2014**, *24*, 151–157. [[CrossRef](#)]
27. Kim, H.-B.; Choi, H.; Jeong, J.; Kim, S.; Walker, B.; Song, S.; Kim, J.Y. Mixed solvents for the optimization of morphology in solution-processed, inverted-type perovskite/fullerene hybrid solar cells. *Nanoscale* **2014**, *6*, 6679–6683. [[CrossRef](#)] [[PubMed](#)]
28. Shen, D.; Yu, X.; Cai, X.; Peng, M.; Ma, Y.; Su, X.; Xiao, L.; Zou, D. Understanding the solvent-assisted crystallization mechanism inherent in efficient organic–inorganic halide perovskite solar cells. *J. Mater. Chem. A* **2014**, *2*, 20454–20461. [[CrossRef](#)]
29. Xiao, M.; Huang, F.; Huang, W.; Dkhissi, Y.; Zhu, Y.; Etheridge, J.; Gray-Weale, A.; Bach, U.; Cheng, Y.-B.; Spiccia, L. A fast deposition-crystallization procedure for highly efficient lead iodide perovskite thin-film solar cells. *Angew. Chem. Int. Ed.* **2014**, *53*, 9898–9903. [[CrossRef](#)] [[PubMed](#)]

30. Nie, W.; Tsai, H.; Asadpour, R.; Blancon, J.-C.; Neukirch, A.J.; Gupta, G.; Crochet, J.J.; Chhowalla, M.; Tretiak, S.; Alam, M.A.; et al. High-efficiency solution-processed perovskite solar cells with millimeter-scale grains. *Science* **2015**, *347*, 522–525. [[CrossRef](#)] [[PubMed](#)]
31. Yang, Y.; Yang, M.; Li, Z.; Crisp, R.; Zhu, K.; Beard, M.C. Comparison of recombination dynamics in $\text{CH}_3\text{NH}_3\text{PbBr}_3$ and $\text{CH}_3\text{NH}_3\text{PbI}_3$ perovskite films: Influence of exciton binding energy. *J. Phys. Chem. Lett.* **2015**, *6*, 4688–4692. [[CrossRef](#)] [[PubMed](#)]
32. Fu, K.; Zhou, Q.; Chen, Y.; Lu, J.; Yang, S.-E. The simulation of physical mechanism for HTM-free perovskite organic lead iodide planar heterojunction solar cells. *J. Opt.* **2015**, *17*, 105904. [[CrossRef](#)]
33. Shao, Y.; Xiao, Z.; Bi, C.; Yuan, Y.; Huang, J. Origin and elimination of photocurrent hysteresis by fullerene passivation in $\text{CH}_3\text{NH}_3\text{PbI}_3$ planar heterojunction solar cells. *Nat. Commun.* **2014**, *5*, 5784. [[CrossRef](#)] [[PubMed](#)]
34. Zhao, Y.; Zhu, K. Optical bleaching of perovskite $(\text{CH}_3\text{NH}_3)\text{PbI}_3$ through room-temperature phase transformation induced by ammonia. *Chem. Commun.* **2014**, *50*, 1605–1607. [[CrossRef](#)] [[PubMed](#)]
35. Zhou, Z.; Wang, Z.; Zhou, Y.; Pang, S.; Wang, D.; Xu, H.; Liu, Z.; Padture, N.P.; Cui, G. Methylamine gas induced defect-healing behavior of $\text{CH}_3\text{NH}_3\text{PbI}_3$ thin films for perovskite solar cells. *Angew. Chem. Int. Ed.* **2015**, *54*, 9705–9709. [[CrossRef](#)] [[PubMed](#)]
36. Chih, Y.-K.; Wang, J.-C.; Yang, R.-T.; Liu, C.-C.; Chang, Y.-C.; Fu, Y.-S.; Lai, W.-C.; Chen, P.; Wen, T.-C.; Huang, Y.-C.; et al. NiO_x Electrode interlayer and $\text{CH}_3\text{NH}_2/\text{CH}_3\text{NH}_3\text{PbBr}_3$ interface treatment to markedly advance hybrid perovskite-based light-emitting diodes. *Adv. Mater.* **2016**, *28*, 8687–8694. [[CrossRef](#)] [[PubMed](#)]
37. Jain, S.M.; Philippe, B.; Johansson, E.M.J.; Park, B.-W.; Rensmo, H.; Edvinsson, T.; Boschloo, G. Frustrated lewis pair-mediated recrystallization of $\text{CH}_3\text{NH}_3\text{PbI}_3$ for improved optoelectronic quality and high voltage planar perovskite solar cells. *Energy Environ. Sci.* **2016**, *9*, 3770–3782. [[CrossRef](#)]
38. Zhao, T.; Williams, S.T.; Chueh, C.-C.; deQuilettes, D.W.; Liang, P.-W.; Ginger, D.S.; Jen, A.K.-Y. Design rules for the broad application of fast (<1 s) methylamine vapor based, hybrid perovskite post deposition treatments. *RSC Adv.* **2016**, *6*, 27475–27484.
39. Jiang, Y.; Juarez-Perez, E.J.; Ge, Q.; Wang, S.; Leyden, M.R.; Ono, L.K.; Raga, S.R.; Hu, J.; Qi, Y. Post-annealing of MAPbI_3 perovskite films with methylamine for efficient perovskite solar cells. *Mater. Horiz.* **2016**, *3*, 548–555. [[CrossRef](#)]
40. Jacobs, D.L.; Zang, L. Thermally induced recrystallization of MAPbI_3 perovskite under methylamine atmosphere: An approach to fabricating large uniform crystalline grains. *Chem. Commun.* **2016**, *52*, 10743–10746. [[CrossRef](#)] [[PubMed](#)]
41. Zhang, T.; Guo, N.; Li, G.; Qian, X.; Li, L.; Zhao, Y. A controllable fabrication of grain boundary PbI_2 nanoplates passivated lead halide perovskites for high performance solar cells. *Nano Energy* **2016**, *26*, 50–56. [[CrossRef](#)]
42. Li, C.; Pang, S.; Xu, H.; Cui, G. Methylamine gas based synthesis and healing process toward upscaling of perovskite solar cells: Progress and perspective. *Sol. RRL* **2017**, *1*, 1700076. [[CrossRef](#)]
43. Wang, Z.-K.; Li, M.; Yang, Y.-G.; Hu, Y.; Ma, H.; Gao, X.-Y.; Liao, L.-S. High efficiency Pb-In binary metal perovskite solar cells. *Adv. Mater.* **2016**, *28*, 6695–6703. [[CrossRef](#)] [[PubMed](#)]
44. Cai, Q.; Li, H.; Jiang, Y.; Tu, L.; Ma, L.; Wu, X.; Yang, S.-E.; Shi, Z.; Zang, J.; Chen, Y. High-efficiency perovskite solar cells based on $\text{MAI}(\text{PbI}_2)_{1-x}(\text{FeCl}_2)_x$ absorber layers. *Sol. Energy* **2018**, *159*, 786–793. [[CrossRef](#)]
45. Liang, C.; Wu, Z.; Li, P.; Fan, J.; Zhang, Y.; Shao, G. Chemical bath deposited rutile TiO_2 compact layer toward efficient planar heterojunction perovskite solar cells. *Appl. Surf. Sci.* **2016**, *391*, 337–344. [[CrossRef](#)]
46. Bisquert, J.; Bertoluzzi, L.; Mora-Sero, I.; Garcia-Belmonte, G. Theory of impedance and capacitance spectroscopy of solar cells with dielectric relaxation, drift-diffusion transport, and recombination. *J. Phys. Chem. C* **2014**, *118*, 18983–18991. [[CrossRef](#)]
47. Suarez, B.; Gonzalez-Pedro, V.; Ripolles, T.S.; Sanchez, R.S.; Otero, L.; Mora-Sero, I. Recombination study of combined halides (Cl, Br, I) perovskite solar cells. *J. Phys. Chem. Lett.* **2014**, *5*, 1628–1635. [[CrossRef](#)] [[PubMed](#)]

